BIOCHEMISTRY
including biophysical chemistry & molecular biology
Article

Biochemistry **2010,** *49,* 1787–1797 1787
DOI: 10.1021/bi902088z

Structure of Epi-Isozizaene Synthase from *Streptomyces coelicolor* A3(2), a Platform for New Terpenoid Cyclization Templates[†,‡]

Julie A. Aaron,[§] Xin Lin,[∥] David E. Cane,*[,∥] and David W. Christianson*[,§]

[§]*Roy and Diana Vagelos Laboratories, Department of Chemistry, University of Pennsylvania, Philadelphia, Pennsylvania 19104-6323, and* [∥]*Department of Chemistry, Box H, Brown University, Providence, Rhode Island 02912-9108*

Received December 5, 2009; Revised Manuscript Received January 20, 2010

ABSTRACT: The X-ray crystal structure of recombinant epi-isozizaene synthase (EIZS), a sesquiterpene cyclase from *Streptomyces coelicolor* A3(2), has been determined at 1.60 Å resolution. Specifically, the structure of wild-type EIZS is that of its closed conformation in complex with three Mg^{2+} ions, inorganic pyrophosphate (PP_i), and the benzyltriethylammonium cation (BTAC). Additionally, the structure of D99N EIZS has been determined in an open, ligand-free conformation at 1.90 Å resolution. Comparison of these two structures provides the first view of conformational changes required for substrate binding and catalysis in a bacterial terpenoid cyclase. Moreover, the binding interactions of BTAC may mimic those of a carbocation intermediate in catalysis. Accordingly, the aromatic rings of F95, F96, and F198 appear to be well-oriented to stabilize carbocation intermediates in the cyclization cascade through cation$-\pi$ interactions. Mutagenesis of aromatic residues in the enzyme active site results in the production of alternative sesquiterpene product arrays due to altered modes of stabilization of carbocation intermediates as well as altered templates for the cyclization of farnesyl diphosphate. Accordingly, the 1.64 Å resolution crystal structure of F198A EIZS in a complex with three Mg^{2+} ions, PP_i, and BTAC reveals an alternative binding orientation of BTAC; alternative binding orientations of a carbocation intermediate could lead to the formation of alternative products. Finally, the crystal structure of wild-type EIZS in a complex with four Hg^{2+} ions has been determined at 1.90 Å resolution, showing that metal binding triggers a significant conformational change of helix G to cap the active site.

The terpenome comprises a chemical library of more than 55000 natural products found in all forms of life that serve a myriad of biological functions. The structural and stereochemical diversity of these terpenoid metabolites derives in large part from the action of terpenoid cyclases, which catalyze the carbocation-mediated cyclization of linear isoprenoids such as the sesquiterpene[1] farnesyl diphosphate (FPP)[2] to generate an enormous variety of cyclic products (*1*−*5*). The active site of a terpenoid cyclase serves as a template for the binding of the flexible acyclic isoprenoid substrate in a unique conformation that permits a specific sequence of bond-making and bond-breaking steps to result in the ultimate formation of a single cyclic product or, as is often the case, a mixture of products generated by the more promiscuous cyclases. Crystal structures of bacterial, fungal, and plant sesquiterpene cyclases[1] determined to date (*6*−*11*) reveal a common α-helical fold similar to that first observed for avian FPP synthase (*12*), despite insignificant amino acid sequence identity among all of these synthases.

In spite of insignificant overall sequence identity, two metal ion binding motifs are universally conserved among terpenoid cyclases: an aspartate-rich motif (**DDXXD/E**) located at the C-terminus of helix D and the "NSE/DTE" motif (**N/DDXXS/TXX(K/R)E**) at the C-terminus of helix H (bold residues are usually metal ligands). The electrophilic cyclization cascade catalyzed by a sesquiterpene cyclase is initiated by the divalent metal ion-dependent ionization of FPP to generate inorganic pyrophosphate (PP_i) and a highly reactive allylic carbocation that can undergo rapid isomerization, cyclization, and rearrangement. X-ray crystallographic studies of sesquiterpene cyclases indicate that significant protein structural changes occur upon the binding of three Mg^{2+} ions and PP_i or FPP analogues to trigger active site closure and substrate ionization, but the details of these structural changes generally differ between plant (*7*, *11*) and fungal (*9*, *10*) sesquiterpene cyclases. Until now, the mechanism of active site closure of a bacterial terpenoid cyclase has remained unknown since the only available crystal structure of a bacterial cyclase has been that of *Streptomyces exfoliatus*

[†]Supported by National Institutes of Health (NIH) Grants GM56838 to D.W.C. and GM30301 to D.E.C. and an NIH Chemistry Biology Interface Training Grant to J.A.A.

[‡]The atomic coordinates and structure factors of wild-type and F198A epi-isozizaene synthase in a complex with three Mg^{2+} ions, inorganic pyrophosphate, and the benzyltriethylammonium cation; wild-type epi-isozizaene synthase in a complex with four Hg^{2+} ions; and ligand-free D99N epi-isozizaene synthase have been deposited in the Protein Data Bank as entries 3KB9, 3LG5, 3KBK, and 3LGK, respectively.

*To whom correspondence should be addressed. D.W.C.: telephone, (215) 898-5714; fax, (215) 573-2201; e-mail, chris@sas.upenn.edu. D.E.C.: telephone, (401) 863-3588; fax, (401) 863-9368; e-mail, david_cane@brown.edu.

[1]A sesquiterpene is a 15-carbon isoprenoid; farnesyl diphosphate is a sesquiterpene formed by the linkage of three five-carbon isoprenoids in a linear, head-to-tail fashion. A sesquiterpene cyclase catalyzes the cyclization of farnesyl diphosphate to form alternative 15-carbon isoprenoid compounds.

[2]Abbreviations: APS, Advanced Photon Source; BME, β-mercaptoethanol; BTAC, benzyltriethylammonium cation; EIZS, epi-isozizaene synthase; FPP, farnesyl diphosphate; LB, Luria-Bertani; PDB, Protein Data Bank; PEG, polyethylene glycol; PP_i, inorganic pyrophosphate; rmsd, root-mean-square deviation; SAD, single-wavelength anomalous dispersion; TCEP, tris(2-carboxyethyl)phosphine; WT, wild-type.

Published on Web 02/04/2010

UC5319 pentalenene synthase, which was determined only in an open, ligand-free conformation (*6*).

Here, we report the first X-ray crystal structure of a bacterial cyclase in a closed active site conformation, recombinant epi-isozizaene synthase (EIZS) from *Streptomyces coelicolor* A3(2). EIZS is related to pentalenene synthase by 24% amino acid sequence identity and catalyzes the multistep cyclization of FPP to form the tricyclic hydrocarbon epi-isozizaene (*13*, *14*). The gene for EIZS is itself transcriptionally coupled to that of cytochrome P450 CYP170A1 (*15*) which performs two sequential allylic oxidations on epi-isozizaene to form albaflavenone, an antibiotic with activity against *Bacillus subtilis* (*16*). We have determined the structure of the EIZS−$Mg^{2+}{}_3$−PP_i−benzyltriethylammonium cation (BTAC) complex at 1.60 Å resolution, as well as the 1.90 Å resolution structure of EIZS in a complex with four Hg^{2+} ions in an unusual closed active site conformation and the 1.90 Å resolution structure of ligand-free D99N EIZS in an open active site conformation. Comparisons of these structures provide new insight regarding the active site closure mechanism of bacterial terpenoid cyclases. Furthermore, mutagenesis of aromatic residues in the EIZS active site results in the production of new sesquiterpene product arrays because of the remolded template for FPP cyclization as well as altered modes of stabilization of carbocation intermediates. Accordingly, we also present the 1.64 Å resolution structure of the F198A EIZS−$Mg^{2+}{}_3$−PP_i−BTAC complex.

MATERIALS AND METHODS

Expression and Purification of Epi-Isozizaene Synthase (EIZS). Recombinant EIZS from *S. coelicolor* A3(2) was expressed at high levels in *Escherichia coli* BL21(DE3) and purified as previously described (*13*) with minor modifications. Briefly, *E. coli* BL21(DE3) carrying pET28a(+)/SCO5222 was inoculated into Luria-Bertani (LB) medium containing kanamycin and grown overnight at 37 °C. A total of 4 L of LB/kanamycin medium was inoculated with 5 mL of the overnight seed culture, and *E. coli* was grown at 37 °C until the OD_{600} reached 0.5. The temperature was reduced to 20 °C, and the cells were induced with 0.1 mM isopropyl β-D-thiogalactopyranoside for 18 h. Cells were harvested, resuspended in 50 mL of Talon buffer A [50 mM sodium phosphate (pH 8.0), 300 mM NaCl, 20% glycerol, and 5 mM β-mercaptoethanol (BME)], supplemented with phenylmethanesulfonyl fluoride and DNase, and sonicated for 6 min using a 40% duty cycle and 30% power range. After three cycles of sonication, the cell lysate was clarified by centrifugation at 16000*g* and 4 °C for 75 min. The clarified lysate was loaded on a Talon Co^{2+} metal affinity resin (5 mL), and a step gradient from 0 to 200 mM imidazole in Talon buffer was applied to elute the enzyme. The fractions were analyzed using SDS−PAGE, and the most concentrated fractions were pooled and applied to a Superdex gel filtration column equilibrated in 20 mM Tris-HCl (pH 7.5), 300 mM NaCl, 10% glycerol, 10 mM $MgCl_2$, and 2 mM tris(2-carboxyethyl)phosphine (TCEP). The fractions were analyzed by SDS−PAGE, and the fractions containing the enzyme were pooled and concentrated to 8 mg/mL enzyme using a YM-10 centricon. The resulting protein preparation was >99% pure on the basis of SDS−PAGE.

Site-Directed Mutagenesis. Single site-specific mutations were introduced into the EIZS wild-type plasmid using primers 1 and 2 for each respective mutant as follows (lowercase letters represent the mutant codon introduced): F96A, 5′-CTA CAG CGC GTG GTT Cgc aGT CTG GGA CGA CCG TC-3′ (primer 1) and 5′-GAC GGT CGT CCC AGA Ctg cGA ACC ACG CGC TGT AG-3′ (primer 2); D99N, 5′-GGT TCT TCG TCT GGa acG ACC GTC ACG AC-3′ (primer 1) and 5′-GTC GTG ACG GTC gtt CCA GAC GAA GAA CC-3′ (primer 2); F198A, 5′-GAA CTG CGC CGG CTC ACG gca GCG CAC TGG ATC TGG AC-3′ (primer 1) and 5′-GTC CAG ATC CAG TGC GCt gcC GTG AGC CGG CGC AGT TC-3′ (primer 2); W203F, 5′-GTT CGC GCA CTG GAT Ctt tAC CGA CCT GCT GG-3′ (primer 1) and 5′-GCT CCA GCA GGT CGG Taa aGA TCC AGT GCG CG-3′ (primer 2). The optimal reaction mixture for PCR amplification of the insert was 100 ng of each forward and reverse primer, 3 μL of 10 mM dNTP mix, 100 ng of plasmid, 5 μL of *Pfu* turbo polymerase buffer, and 1 unit of *Pfu* turbo polymerase diluted with water to a final volume of 50 μL. Optimal PCR conditions required initial denaturation of the reaction mixture at 95 °C for 5 min, addition of polymerase followed by 30 cycles (denaturation for 1 min at 95 °C, annealing for 1 min at 60 °C, and extension for 8 min at 72 °C), and a final 10 min extension at 72 °C followed by a final hold at 4 °C. One microliter of Dpn1 was added to the PCR mixture and incubated at 37 °C for 1 h to digest the template. PCR products were transformed into XL1-Blue cells for DNA isolation and sequencing. DNA was purified (Qiagen mini-prep kit) from cultures from single colonies, and DNA sequencing (DNA Sequencing Facility, University of Pennsylvania) confirmed incorporation of the mutations. Mutant proteins were expressed and purified using the same procedures described above for the wild-type enzyme.

Crystallization and Determination of the Structure of the EIZS−$Mg^{2+}{}_3$−PP_i−BTAC Complex. EIZS was crystallized by the sitting drop vapor diffusion method. Typically, a 4 μL drop of protein solution [8−10 mg/mL EIZS, 20 mM Tris-HCl (pH 7.5), 300 mM NaCl, 10 mM $MgCl_2$, 10% glycerol, 2 mM TCEP, 2 mM sodium pyrophosphate, and 2 mM benzyltriethylammonium chloride] was added to 4 μL of precipitant solution [100 mM Bis-Tris (pH 5.5), 25−28% polyethylene glycol 3350, and 0.2 M $(NH_4)_2SO_4$] and equilibrated against a 1 mL well reservoir of precipitant solution. Crystals appeared within 2−3 days and grew to maximal dimensions of 100 μm × 10 μm × 10 μm. Crystals diffracted X-rays to 1.60 Å resolution at the Advanced Photon Source (Argonne, IL), beamline NE-CAT 24-ID-C, and belonged to space group $P2_1$ with one monomer in the asymmetric unit, a Matthews coefficient (V_M) of 2.1 $Å^3$/Da, corresponding to a solvent content of 43%, and the following unit cell parameters: a = 53.185 Å, b = 47.374 Å, c = 75.376 Å, and β = 95.53°.

Heavy-atom derivatives were prepared by soaking crystals in precipitant buffer supplemented with 1 mM ethylmercury chloride for 1−2 days. Diffraction data were collected at the absorption edge of mercury (1.0548 Å) on beamline X29 at the National Synchrotron Light Source (NSLS). Crystals diffracted X-rays to 1.90 Å and belonged to space group $P2_1$ with the following unit cell parameters: a = 51.693 Å, b = 46.549 Å, c = 75.551 Å, and β = 92.34°. Data reduction was achieved with Denzo and Scalepack (*17*). Difference Patterson maps generated with anomalous scattering data revealed large peaks corresponding to mercury. The initial electron density map was phased by single-wavelength anomalous dispersion (SAD) of mercury using autoSHARP (*18*). Following density modification and automatic building, approximately 50% of the protein residues were built

Table 1: Data Collection and Refinement Statistics

	EIZS−$Mg^{2+}{}_3$−PP_i−BTAC complex	EIZS−$Hg^{2+}{}_4$ complex	F198A EIZS−$Mg^{2+}{}_3$−PP_i−BTAC complex	D99N EIZS (ligand-free)
		Data Collection		
wavelength (Å)	1.0080	1.0548	1.075	0.9795
resolution (Å)	40−1.60	50−1.90	50−1.64	50−1.90
no. of unique reflections	46113	28446	45831	28694
completeness[a] (%)	92.9 (100)	99.4 (98.6)	99.8 (100)	97.6 (95.6)
redundancy[a]	3.6 (3.6)	5.1 (5.1)	3.6 (3.5)	3.3 (3.0)
$R_{sym}{}^{a,b}$	0.058 (0.208)	0.075 (0.325)	0.062 (0.238)	0.089 (0.634)
		Refinement		
$R_{cryst}/R_{free}{}^{c}$	0.158/0.189	0.169/0.202	0.156/0.190	0.162/0.207
rmsd for bonds (Å)	0.012	0.005	0.015	0.009
rmsd for angles (deg)	1.4	0.8	1.6	1.1
rmsd for dihedral angles (deg)	21	15	18	16
no. of atoms				
protein	2858	2512	2858	2638
solvent	431	335	467	316
ligand	55	13	31	5
Ramachandran plot (%)				
allowed	94.7	95.2	95.0	94.4
additionally allowed	5.3	4.8	5.0	5.6

[a]Values in parentheses refer to the highest-resolution shell. [b]$R_{sym} = \sum|I_h - \langle I_h\rangle|/\sum I_h$, where $\langle I_h\rangle$ is the average intensity over symmetry equivalent refections. [c]$R_{cryst} = \sum||F_{obs}| - |F_{calc}||/\sum|F_{obs}|$, where summation is over the data used for refinement. R_{free} was calculated as described for R_{cryst} by using 5% of the data excluded from refinement.

into the electron density map. At this point, the molecular model of EIZS was refined against the 1.60 Å resolution data set collected from the native crystal instead of the mercury derivative. Iterative cycles of refinement and manual model building using CNS (*19*), O (*20*), COOT (*21*), and PHENIX (*22*) allowed for the assembly of the complete protein model. Individual atomic *B* factors were utilized during refinement. Buffer molecules, ions, water, glycerol, the benzyltriethylammonium cation (BTAC), PP_i, and a sulfate ion (hydrogen bonded to R163, H164, R220, and R226) were included in later cycles of refinement. Data reduction and refinement statistics are listed in Table 1. A total of 340 of 381 residues (A16−N355) are present in the final model, as the N- and C-termini are disordered.

Determination of the Crystal Structure of the F198A EIZS−$Mg^{2+}{}_3$−PP_i−BTAC Complex. The F198A EIZS mutant was crystallized by the hanging drop vapor diffusion method with the same conditions used to crystallize the wild-type enzyme, but with successive rounds of microstreak seeding using native crystals as the seed stock. Crystals diffracted to 1.64 Å resolution at NSLS beamline X29 and belonged to space group $P2_1$ with the following unit cell parameters: $a = 53.241$ Å, $b = 47.179$ Å, $c = 75.568$ Å, and $\beta = 95.57°$. Molecular replacement calculations were performed with PHASER (*23*) using the atomic coordinates of native EIZS (less ligands and solvent atoms) as a search probe. The electron density clearly revealed the F198A mutation. Iterative cycles of refinement and manual model building were achieved with PHENIX and COOT, respectively. Ions, PP_i, BTAC, and water molecules were included in later cycles of refinement. Individual atomic *B* factors were utilized.

Determination of the Crystal Structure of the EIZS−$Hg^{2+}{}_4$ Complex. To investigate the mercury binding sites of the ethylmercury chloride-derivatized crystals used for structure determination, refinement of the 1.90 Å resolution structure was completed. Four mercury binding sites were identified by strong peaks in a Bijvoet difference Fourier map adjacent to C68, C213, C243, and C283. Iterative cycles of refinement and manual model building were achieved with PHENIX and COOT, respectively. Ions and water molecules were included in later cycles of refinement. Individual atomic *B* factors were utilized, and the mercury, chloride, and sulfur atoms were refined anisotropically. Data reduction and refinement statistics are listed in Table 1. A total of 323 of 381 residues are present in the final model, as there was no interpretable density for the A251−L267 loop as well as the N- and C-termini.

Determination of the Crystal Structure of Ligand-Free D99N EIZS. The D99N EIZS mutant was crystallized by the hanging drop vapor diffusion method. Crystals formed with a precipitant solution at a pH slightly higher than that of the wild-type crystals [100 mM Bis-Tris (pH 6.0), 25−28% polyethylene glycol 3350, and 0.2 M $(NH_4)_2SO_4$] and were improved by successive rounds of microstreak seeding using D99N crystals as the seed stock. Crystals diffracted to 1.9 Å resolution at APS beamline NE-CAT 24-ID-C and belonged to space group $P2_12_12_1$ with the following unit cell parameters: $a = 41.144$ Å, $b = 81.952$ Å, and $c = 106.693$ Å. Molecular replacement calculations were performed with PHASER using the atomic coordinates of native EIZS (less ligand and solvent atoms) as a search probe. Iterative cycles of refinement and manual model building were achieved with PHENIX and COOT, respectively. Sulfate, glycerol, and water molecules were included in later cycles of refinement. Individual atomic *B* factors were utilized. Data reduction and refinement statistics are listed in Table 1. A total of 316 of 381 residues (P18−E335) are present in the final model, as the N- and C-termini are disordered.

Determination of Kinetic Parameters of EIZS Mutants. EIZS mutants were assayed as previously described (*13*) in 50 mM piperazine-*N*,*N*′-bis(2-ethanesulfonic acid) (PIPES) (pH 6.5), 20% glycerol, 100 mM NaCl, 10 mM $MgCl_2$, and 5 mM BME. Each series of assays was performed two or three times using concentrations of [1-^{3}H]FPP (100 mCi/mmol) ranging

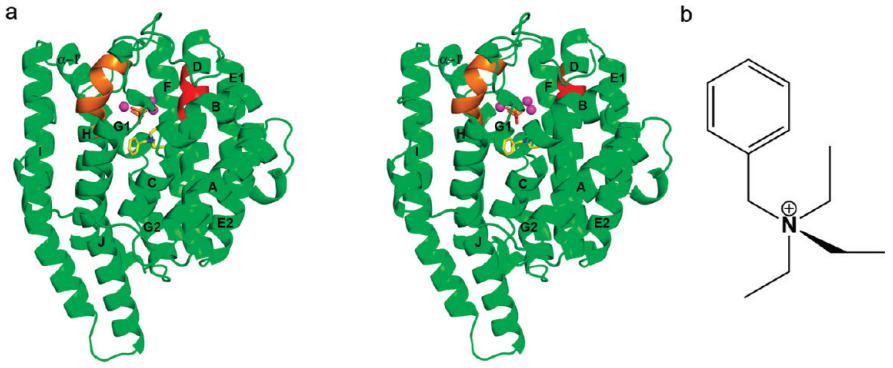

FIGURE 1: (a) Ribbon plot of the EIZS−$Mg^{2+}{}_3$−PP_i−BTAC complex showing the aspartate-rich motif (red) and the NSE motif (orange) flanking the mouth of the active site. The Mg^{2+} ions are shown as magenta spheres, and PP_i and BTAC molecules are color-coded by atom (yellow for carbon, blue for nitrogen, red for oxygen, and orange for phosphorus). Helices are labeled according to the convention first established for FPP synthase (*12*). (b) The quaternary ammonium group of the benzyltriethylammonium cation (BTAC) serves as a mimic of a carbocation intermediate in catalysis.

from 0.025 to 50 μM. The optimal enzyme concentration for each mutant was determined, where the dependence of product formation on enzyme concentration was linear and less than 10% of the substrate was turned over: wild type (1 nM), F96A, F198A, and W203F (20 nM). A 1 mL reaction mixture in a test tube was overlaid with 1 mL of hexane immediately after addition of substrate, covered with aluminum foil, and incubated for 15 min at 30 °C. The reaction was quenched by addition of 75 μL of 500 mM EDTA (pH 8.0) and the mixture vortexed for 20 s. The hexane extract was passed through a silica gel column directly into a scintillation vial containing 5 mL of scintillation fluid. The aqueous phase was extracted with an additional 2 × 1 mL of hexane and passed through the same silica gel column. Finally, the column was washed with an additional 1 mL of hexane. A Beckman scintillation counter was used to measure product formation, and the substrate concentration versus rate of product formation data were fit by nonlinear regression using Prism to determine k_{cat} based on the known total enzyme concentration.

Analysis of Product Arrays Generated by EIZS Mutants. Substrate farnesyl diphosphate (60 μM) was incubated with 40 μM mutant EIZS (F96A, F198A, or W203F) in 6 mL of buffer (50 mM PIPES, 15 mM $MgCl_2$, 100 mM NaCl, 20% glycerol, and 5 mM BME) and overlaid with 3 mL of HPLC-grade *n*-pentane in a glass test tube at 30 °C for 18 h. Reaction products were extracted with *n*-pentane three times, dried with anhydrous $MgSO_4$, and concentrated on an ice/water mixture under reduced pressure until the volume was reduced to 100 μL. The products were analyzed using an Agilent 6890 GC/JEOL JMS-600H mass spectrometer, using a 30 m × 0.25 mm HP5MS capillary column (Department of Chemistry, Brown University) in EI (positive) mode using a temperature program of 60−280 °C, with a gradient of 20 °C/min and a solvent delay of 3.5 min. Analysis of the organic extracts resulting from the incubation of FPP with the mutant cyclases by gas chromatography and mass spectrometry (GC−MS) reveals the formation of mixtures of sesquiterpene hydrocarbons with *m*/*z* 204. Compounds were identified by comparison of their individual mass spectra and chromatographic retention indices with those of authentic compounds in the MassFinder 3.0 Database (*24*).

RESULTS AND DISCUSSION

Structure of the EIZS−$Mg^{2+}{}_3$−PP_i−BTAC Complex. At 1.60 Å resolution, the crystal structure of this complex is the highest-resolution structure of any terpenoid cyclase determined to date. EIZS adopts the class I terpenoid synthase α-helical fold and consists of a bundle of 10 α-helices, designated A−J (Figure 1a), in which the 20 Å deep active site is defined mainly by helices C, D, G, H, and J. Among the terpenoid cyclases of known structure, EIZS is structurally most similar to pentalenene synthase (rmsd of 3.3 Å for 304 Cα atoms). EIZS crystallizes as a monomer, consistent with dynamic light scattering measurements indicating that the protein is a monomer in solution (data not shown).

The electron density map clearly reveals three Mg^{2+} ions, PP_i, and a BTAC molecule bound in the active site (Figure 2a; for reference, the molecular structure of BTAC is illustrated in Figure 1b). The side chain of D99 in the aspartate-rich **D**^{99}DRHD^{103} motif coordinates to $Mg^{2+}{}_A$ and $Mg^{2+}{}_C$ with *syn*,*syn*-bidentate geometry, while $Mg^{2+}{}_B$ is chelated by the NSE **N**^{240}DLCSLPK**E**^{248} motif (bold indicates Mg^{2+} ligands). Each Mg^{2+} ion is coordinated with octahedral geometry, with nonprotein coordination sites occupied by the oxygen atoms of PP_i and by water molecules. The PP_i anion also accepts hydrogen bonds from the side chains of R194, K247, R338, and Y339 (Figure 2b). It is likely that similar metal coordination and hydrogen bond interactions are normally formed with the diphosphate group of the substrate FPP in the precatalytic Michaelis complex. These interactions stabilize the closed active site conformation that sequesters FPP from bulk solvent and triggers ionization to initiate the electrophilic cyclization cascade.

Interestingly, the detailed structural changes that occur between open and closed active site conformations differ between fungal and plant terpenoid cyclases. For example, the rmsd between ligand-free and trichodiene synthase from *Fusarium sporotrichioides* in a complex with $Mg^{2+}{}_3$ and PP_i is 1.4 Å (*9*), whereas that of bornyl diphosphate synthase from *Salvia officinalis* (culinary sage) is only 0.6 Å for the catalytic domain (*25*). Until now, the structure of the closed conformation of a bacterial terpenoid cyclase has remained unknown because the only other bacterial terpenoid cyclase crystal structure, that of pentalenene synthase, had been determined only in the ligand-free state (*6*). Importantly, the residues that interact with Mg^{2+} ions or PP_i in EIZS are conserved in pentalenene synthase. Superposition of the closed, ligand-bound structure of EIZS with ligand-free pentalenene synthase reveals a very similar alignment of the metal binding motifs, with pentalenene synthase helices D and H being 1.5 Å farther apart than in EIZS. We hypothesize that upon

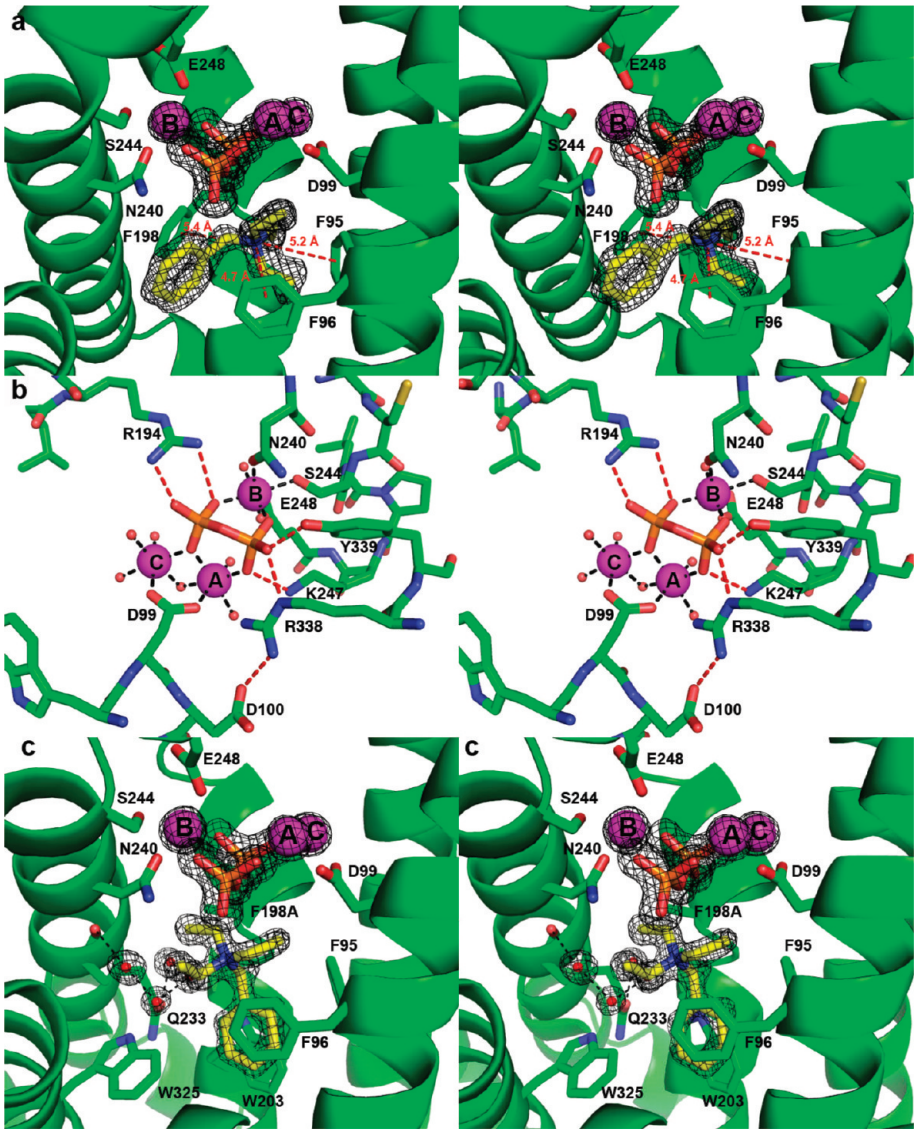

FIGURE 2: (a) Simulated annealing omit maps (black) of the PP_i anion, Mg^{2+} ions, and BTAC, contoured at 5σ. Note the cation$-\pi$ interactions between the positively charged quaternary ammonium group of BTAC and the aromatic rings of F95, F96, and F198 (red dashed lines). (b) Metal coordination interactions (black dashed lines) and hydrogen bond interactions (red dashed lines) in the EIZS$-{Mg^{2+}}_3-PP_i$ complex. (c) Simulated annealing omit maps (black) of the PP_i anion, Mg^{2+} ions, and BTAC in the active site of F198A EIZS, contoured at 5σ. Note the alternative position of BTAC resulting from the F198A mutation.

binding of ${Mg^{2+}}_3$ and substrate or PP_i, the active site of pentalenene synthase undergoes a change to a closed conformation comparable to that observed for the EIZS$-{Mg^{2+}}_3-PP_i-$BTAC complex.

Although the first and third aspartate residues in the aspartate-rich metal binding motif coordinate to ${Mg^{2+}}_A$ and ${Mg^{2+}}_C$ in the plant terpenoid cyclases containing a complete trinuclear metal cluster such as (+)-bornyl diphosphate synthase (*25*), limonene synthase (*26*), and (+)-δ-cadinene synthase (*11*), only the first aspartate residue in this motif coordinates to ${Mg^{2+}}_A$ and ${Mg^{2+}}_C$ in complexes of the fungal cyclases trichodiene synthase (*9*) and aristolochene synthase (*10*) with ${Mg^{2+}}_3$ and PP_i. EIZS is similar to the fungal cyclases in that only D99 coordinates to ${Mg^{2+}}_A$ and ${Mg^{2+}}_C$. A critical role for D99 in metal complexation is reflected in the dramatic losses of catalytic activity measured for the D99N and D99E mutants (*14*). Although D100 of EIZS does not directly interact with the Mg^{2+} ions or PP_i, it does accept a hydrogen bond from R338, which also donates a hydrogen bond to PP_i (Figure 2b). Site-directed mutagenesis reveals that the D100N mutant has lost >95% of its activity compared to the native enzyme (*14*), suggesting that the D100N mutation disrupts the D100$-$R338$-PP_i$ hydrogen bond network. In trichodiene synthase, the second aspartate in the aspartate-rich motif, D101, similarly stabilizes a hydrogen bond network with R304 and PP_i (*9*), suggesting that the bacterial and fungal cyclases share the same molecular strategy for linking the molecular recognition of the substrate diphosphate group with the mechanism of active site closure.

Similar analysis of the steady-state kinetic parameters of pentalenene synthase mutated in the aspartate-rich motif (*27*) has established that the first aspartate in the DDLFD segment has the largest effect on catalytic activity, with the D80E substitution resulting in an ~3500-fold reduction in k_{cat}/K_M. By contrast, the D81E substitution results in a more modest 400-fold reduction in k_{cat}/K_M (*27*). Notably, the D84E substitution results in an only ~3-fold reduction in k_{cat}/K_M, consistent with the finding that in EIZS the corresponding third aspartate in the DDxxD motif points away from the active site and is not involved

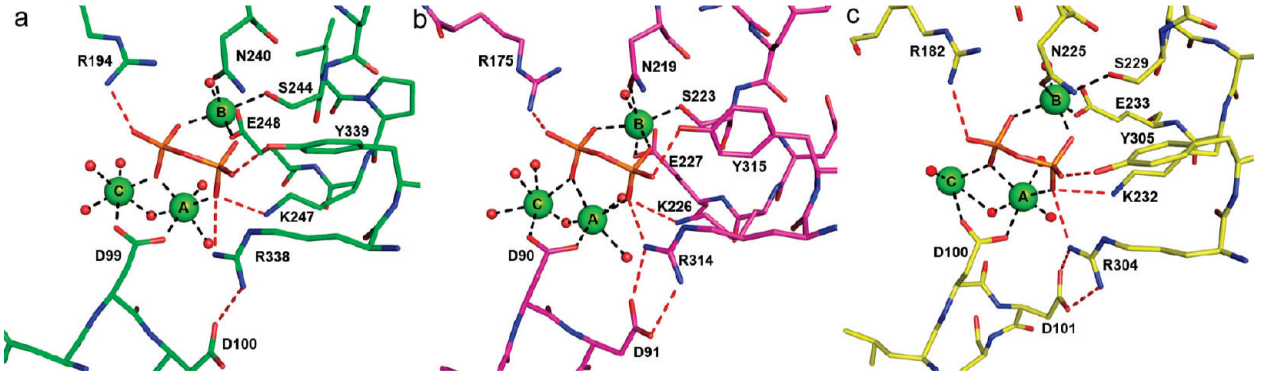

FIGURE 3: Mg^{2+}_3–PP_i binding motif that is conserved among the bacterial and fungal sesquiterpene cyclases otherwise related by < 20% amino acid sequence identity: (a) EIZS from *S. coelicolor* A3(2) (PDB entry 3KB9), (b) aristolochene synthase from *Aspergillus terreus* (PDB entry 2OAB, monomer D), and (c) trichodiene synthase from *F. sporotrichioides* (PDB entry 1JFG, monomer B).

in substrate binding. Thus, the structure of the EIZS–Mg^{2+}_3–PP_i–BTAC complex, as well as mutagenesis results with both EIZS (*14*) and pentalenene synthase (*27*), suggests that the third aspartate in the DDxxD motif of bacterial terpenoid cyclases is not involved in metal binding or essential for catalysis. Remarkably, the molecular recognition of Mg^{2+}_3–PP_i is conserved among fungal cyclases such as aristolochene synthase and trichodiene synthase, and bacterial cyclases, such as EIZS, that otherwise bear no significant overall amino acid sequence relationship (Figure 3).

Crystals of EIZS form upon addition of BTAC (Figure 1b), commonly used in synthetic organic chemistry as a phase transfer catalyst. As a hydrophobic cation, BTAC mimics the bisabolyl carbocation intermediate proposed for the EIZS-catalyzed cyclization mechanism (*13*). The positively charged quaternary ammonium group of BTAC appears to be stabilized by long-range electrostatic interactions with the PP_i anion (the shortest N–O separation is 4.1 Å), as well as cation–π interactions with the aromatic side chains of F95, F96, and F198 (N–ring centroid separations range from 4.7 to 5.4 Å) (Figure 2a). Such cation–π interactions are proposed to play a critical role in stabilizing the highly reactive carbocation intermediates found in all enzyme-catalyzed terpenoid cyclizations (*6*, *28*, *29*). The binding of BTAC in the active site of EIZS demonstrates that the bacterial terpenoid cylase active site can accommodate and stabilize a positively charged ligand resembling the positively charged carbocation intermediates of the normal cyclization cascade. Although determined at a much lower resolution of 2.85 Å, the recently reported structure of the trichodiene synthase–Mg^{2+}_3–PP_i–BTAC complex provides an example of the stabilization of positively charged ligands in the active site of a fungal terpenoid cyclase (*30*).

Structures of the EIZS–Hg^{2+}_4 Complex and D99N EIZS. To date, we have been unable to prepare crystals of wild-type EIZS in a completely ligand-free state, since additives BTAC and PP_i required for crystallization are not readily dialyzed out of the crystals. However, soaking crystals of the EIZS–Mg^{2+}_3–PP_i–BTAC complex with ethylmercury chloride displaces three Mg^{2+} ions, PP_i, and BTAC to yield the 1.90 Å resolution structure of the EIZS–Hg^{2+}_4 complex in which all Hg^{2+} ions bind remotely from the active site (Figure 4a). In this complex, Hg^{2+}_A is coordinated by C68, Hg^{2+}_B is coordinated by C283 (the electron density is best interpreted as two alternate positions), Hg^{2+}_C is coordinated by C243, and Hg^{2+}_D is coordinated by C213 (two alternate positions). Surprisingly, however, the now ligand-free active site is not open and empty, as it is in all other ligand-free terpenoid cyclase structures. Instead, helix G, which forms one side of the active site (and contains R194, a residue that donates a hydrogen bond to PP_i in the ligand-bound structure), bends by ~110° to occupy the location formerly occupied by the Mg^{2+}_3–PP_i binding motif (Figure 4b). Additionally, helix D moves ~1.5 Å outward, helix J moves ~4 Å outward, while helix H, which was bent in the ligand-bound structure to enable Mg^{2+}_B chelation by the NSE motif, becomes straight and also moves outward (Figure 4a). The positions and conformations of helices C, E, and F remain essentially unchanged, and there is no interpretable electron density for helix I or the loop (A251–L267) connecting it to helices H and J. Salt bridges between helix G and helices D and F stabilize the closed ligand-free structure: R194 makes a salt bridge with E175 (helix F), and R195 makes a salt bridge with D103 (helix D) (Figure 4b). Although these residues are found in pentalenene synthase as R173, F174, D84, and E152, a comparable closed ligand-free conformation was not observed by Lesburg and colleagues (*6*). The role of the Hg^{2+} ions in dislodging the Mg^{2+}_3–PP_i–BTAC binding motif to result in the closed ligand-free conformation of EIZS is unclear; inspection of the mercury binding sites does not reveal any particular structural changes that would trigger the observed change in the conformation of helix G.

To further explore structural changes resulting from the dissociation of the Mg^{2+}_3–PP_i–BTAC binding motif from the active site of EIZS, we determined the structure of D99N EIZS at 1.9 Å resolution. This amino acid substitution compromises the *syn*,*syn*-bidentate coordination of Mg^{2+}_A and Mg^{2+}_C (Figure 2b) and consequently diminishes catalytic efficiency (*14*). The crystal structure reveals the complete absence of the Mg^{2+}_3–PP_i–BTAC binding motif in the active site. Moreover, the active site of D99N EIZS adopts an open conformation (Figure 4c) without any conformational changes in helix G. Therefore, we conclude that the conformational change of helix G shown in panels a and b of Figure 4 is somehow caused by Hg^{2+} binding. Comparison of the structures of ligand-free D99N EIZS and the EIZS–Mg^{2+}_3–PP_i–BTAC complex reveals ligand-induced conformational changes in helix H and loop H-α-1, as well as the J–K loop (which is completely disordered in D99N EIZS) (Figure 4c). The overall rmsd between wild-type and D99N EIZS structures is 1.6 Å for 318 Cα atoms.

Structure of the F198A EIZS–Mg^{2+}_3–PP_i–BTAC Complex. To investigate structural changes in the active site resulting from mutagenesis of aromatic residues, we determined the X-ray crystal structure of F198A EIZS at 1.64 Å resolution. This mutant was selected for X-ray crystallographic study

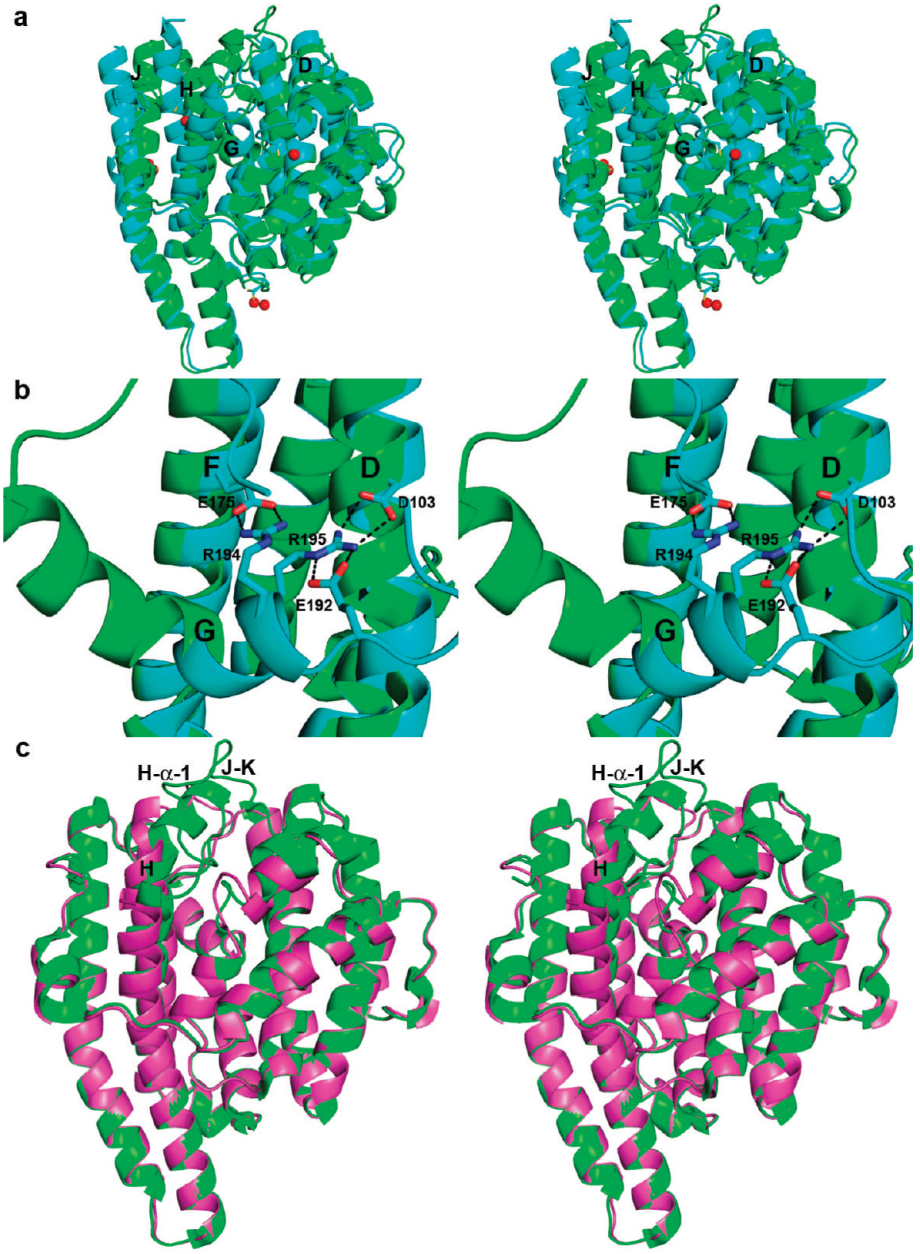

FIGURE 4: (a) Superposition of ribbon plots of the EIZS−$Mg^{2+}{}_3$−PP_i−BTAC (green) and EIZS−$Hg^{2+}{}_4$ (cyan; Hg^{2+} ions appear as red spheres) complexes. Helices D, G, H, and J, which undergo the largest changes, are labeled. (b) Salt bridges (black dashes) between helix G and helices D and F stabilize the closed ligand-free structure. (c) Superposition of the EIZS−$Mg^{2+}{}_3$−PP_i−BTAC complex (green) and D99N EIZS (purple), illustrating the structural changes in helix H and the H-α-1 and J−K loops that accompany active site closure.

because it retains some catalytic activity (Table 2) and exhibits a remarkably altered product array (Table 3) (vide infra). Overall, the F198A mutation results in minimal structural perturbations, and the rmsd between the structure of wild-type EIZS and F198A EIZS is 0.10 Å for 340 Cα atoms. In the active site, the largest structural changes resulting from the F198A substitution are an ~30° rotation of the side chain of F95 and an alternative rotamer of M73. The binding mode of the $Mg^{2+}{}_3$−PP_i binding motif is identical to that observed in the wild-type enzyme; however, the BTAC molecule occupies an alternative position such that its benzyl ring makes quadrupole−quadrupole interactions with the aromatic rings of F95, F96, W203, and W325 (Figure 2c). Surprisingly, four solvent molecules are observed in the active site, forming a hydrogen bonding network with N233 and the backbone carbonyl of A236.

Table 2: Steady-State Kinetic Parameters for Wild-Type EIZS and Site-Specific Mutants

protein	k_{cat} (s^{-1})	K_M (nM)	k_{cat}/K_M (M^{-1} s^{-1})
WT	0.045 ± 0.003	710 ± 100	(6.3 ± 0.1) × 10^4
F96A	0.00024 ± 0.00002	770 ± 130	310 ± 60
F198A	0.00030 ± 0.00002	1200 ± 200	250 ± 45
W203F	0.00034 ± 0.00003	1450 ± 240	230 ± 40

Activity of Aromatic Mutants and Altered Product Arrays. Mutagenesis of residues that coordinate to metal ions or donate hydrogen bonds to the substrate diphosphate group can significantly compromise catalysis by a terpenoid cyclase. For example, mutation of EIZS metal-binding residues can result in a >95% decrease in cyclase activity, as well as altered ratios of aberrant cyclization products (*14*). Amino acid substitutions that

Table 3: Distribution of Sesquiterpene Products for Wild-Type EIZS and Site-Specific Mutants

	relative product percentage (%)													
protein	unknown A	sesquisabine	β-farnesene	epi-isozizaene	zizaene	β-acoradiene	Z-α-bisabolene	sesqui-phellandrene	Z-γ-bisabolene	unknown B	unknown C	unknown D	unknown E	α-cedrene
WT	–	2	5	79	9		–	1	–	–	–	–	–	2
F96A	7	9	70	8	–	–	–	–	7	–	–	–	–	–
F198A	6	20	5	–	–	12	6	13	24	–	7	7	–	–
W203F	4	7	6	14	7	–	–	–	47	6	–	8	3	–

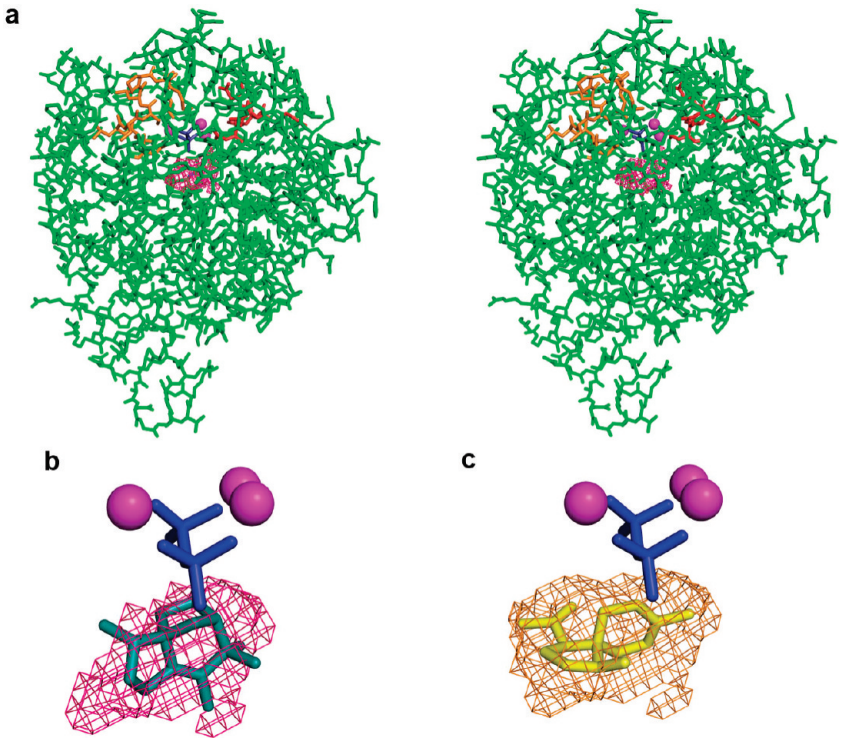

FIGURE 5: (a) Stereoview of the active site surface contour encapsulated by the closed conformation of EIZS shown as a magenta mesh. The aspartate-rich motif (red) and the NSE motif (orange) are oriented as in Figure 1. (b) Cyclization product, epi-isozizaene, modeled into the enclosed active site contour of EIZS (magenta mesh), and the location of the $Mg^{2+}{}_3$–PP_i cluster is shown as a visual reference. (c) Enclosed active site contour of F198A EIZS (light brown meshwork) into which the new cyclization product β-acoradiene is modeled. The remolded active site contour in this mutant prevents epi-isozizaene formation but permits the formation of new or alternative sesquiterpene products predominantly derived from the bisabolyl carbocation intermediate.

change the contour and electronic environment of the active site can alter the product profile of a terpenoid cyclase even more dramatically. The crystal structure of EIZS reveals that the active site contour is defined by hydrophobic and aromatic residues that, when locked in the closed conformation by three Mg^{2+} ions and the substrate diphosphate group, create a unique template that preferentially chaperones the cyclization of FPP to form epi-isozizaene (Figure 5). The active site contour appears to be product-like in shape, although it does not appear to be as complementary a fit as, for example, that between the closed active site contour of the *A. terreus* aristolochene synthase and its sesquiterpene product (*10*). This is a possible signal of catalytic promiscuity, in that wild-type EIZS generates 80% epi-isozizaene and 20% of a mixture of alternative sesquiterpene products (*14*). While a less-perfect template can result in the formation of multiple products, the active site contour of a terpenoid cyclase can be further remolded by structure-based site-directed mutagenesis to permit greater product diversity.

As the first step in exploring the importance of active site aromatic residues for catalysis and product diversity in EIZS, we have prepared the F96A, F198A, and W203F mutants. These residues were selected for mutation on the basis of their proximity to the BTAC cation (Figure 2). Steady-state kinetic parameters measured for these mutants (Table 2) indicate that the mutations only modestly affect K_M but more significantly affect k_{cat}. Accordingly, overall catalytic efficiencies (k_{cat}/K_M) are decreased 205−275-fold. Notably, none of the three active site aromatic mutants generate epi-isozizaene as a major product; indeed, no epi-isozizaene whatsoever is generated by the F198A mutant, and the active site contour of this variant as observed in the crystal structure of the F198A EIZS−$Mg^{2+}{}_3$–PP_i−BTAC complex is more complementary in shape to bisabolene-derived cyclization products such as β-acoradiene, as illustrated in Figure 5. Notably, β-acoradiene is not generated by wild-type EIZS, so the appearance of this spiroterpenoid represents a new catalytic activity introduced by a single amino acid substitution. Altering the active site contour of EIZS alters the conformations and cyclization trajectories of FPP and reactive carbocation intermediates, and the formation of alternative products appears to depend on how well a particular alternative product fits the

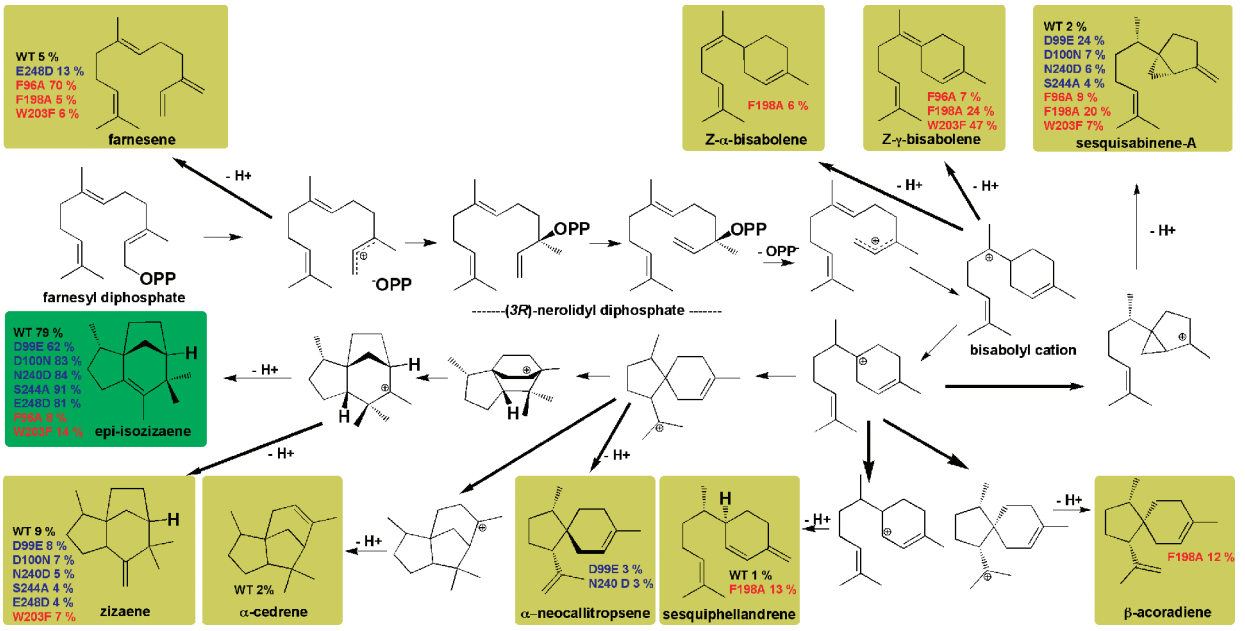

FIGURE 6: Biosynthetic versatility of EIZS can be manipulated by site-directed mutagenesis, as illustrated for sesquiterpene products identified for wild-type (WT) and mutant cyclases. In general, more diverse sesquiterpene product arrays result from the substitution of aromatic residues defining the active site contour (red labels) than from substitution of residues that coordinate the Mg^{2+} ions required for catalysis [blue labels (*14*)]. For example, F198A EIZS does not generate epi-isozizaene at all but instead generates a mixture of sesquisabinene A, *Z*-α- and *Z*-γ-bisabolenes, sesquiphellandrene, and *β*-acoradiene as its major cyclization products. Remolding the active site contour permits the generation of alternative products as long as they can be accommodated within the remolded template, as illustrated for *β*-acoradiene in Figure 5. It is interesting to note that many of these reactions have been examined in theoretical and computational studies (*33*).

remolded active site contour in a mutant cyclase. Additionally, the F96A and F198A substitutions could compromise the potential stabilization of carbocation intermediates by cation−*π* interactions. Some of the sesquiterpenes generated by these aromatic mutants have previously been observed as side products generated by both wild-type and mutant EIZS enzymes (*14*), while three sesquiterpene products have not previously been observed with this cyclase (Figure 6 and Table 3).

(*E*)-*β*-Farnesene, the major product (70%) formed by F96A EIZS, results from deprotonation at C-3[1] of the allylic cation that results from the initial ionization of FPP; other reaction products include sesquisabinene A, *Z*-γ-bisabolene, and an unidentified hydrocarbon presumed to be a sesquiterpene based on mass spectrometry, with *m*/*z* 204. F198A EIZS generates sesquisabinene A, (*E*)-*β*-farnesene, zizaene, *β*-acoradiene, *Z*-α-bisabolene, sesquiphellandrene, *Z*-γ-bisabolene, and three unidentified sesquiterpenes. Interestingly, F198A EIZS generates no epi-isozizaene. The predominant product of W203F EIZS is *Z*-γ-bisabolene, generated by the abstraction of a proton from the intermediate bisabolyl cation (Figure 6). Epi-isozizaene accounts for 14% of the products of the W203F mutant; the remaining products include sesquisabinene, (*E*)-*β*-farnesene, zizaene, and four unidentified sesquiterpenes. It is notable that epi-isozizaene biosynthetic activity is preserved, if only partially so, in the EIZS mutant with the most conservative aromatic−aromatic substitution, which presumably preserves more of the general contour and electrostatic profile of the active site.

CONCLUDING REMARKS

The crystal structures of the EIZS−$Mg^{2+}{}_3$−PP_i−BTAC complex and D99N EIZS are particularly informative in that they reveal two active site conformations: a closed, ligand-bound conformation and an open, ligand-free conformation, respectively. Comparison of these structures reveals, for the first time, conformational changes that occur upon ligand binding in bacterial sesquiterpene cyclases. In the closed, ligand-bound conformation, only the first aspartate of the **D**[99]DRHD motif coordinates to $Mg^{2+}{}_A$ and $Mg^{2+}{}_C$; substitution of a neutral asparagine residue for the negatively charged aspartate residue at position 99 is sufficient to disrupt the assembly and stability of the trinuclear metal cluster required for substrate recognition and activation. Conformational changes that accompany active site closure in the bacterial cyclase involve helix H and the H-α-1 loop, and the J−K loop at the C-terminus (Figure 4c). Corresponding structural changes generally accompany active site closure in fungal (*31*) and plant (*25*) terpenoid cyclases. The template for FPP cyclization is fully formed in the closed active site conformation of EIZS as well as all other class I terpenoid cyclases.

In general, the permissiveness and promiscuity of terpenoid cyclases vary, both in terms of the substrates they accept and the product(s) they generate. These properties are dictated by the three-dimensional contour of the fully formed template in the closed active site conformation. Many terpenoid cyclases, such as *A. terreus* aristolochene synthase (*32*), are high-fidelity cyclases that generate one product exclusively. However, other cyclases such as EIZS generate one major product and (usually) minor quantities of one or more alternative products (*14*). The structural basis for such mechanistic promiscuity is presumably rooted in how well the active site contour enforces the correct regiochemistry and stereochemistry for cyclization and eventual quenching of the carbocation intermediates by chaperoning the conformations of reactive intermediates. Intriguingly, the conformations and orientations of such intermediates may not reflect the original conformation and orientation of the substrate if the template is somewhat permissive (*33*). A more permissive template allows alternative premature quenching of on-pathway intermediates or

off-pathway conformations that lead to the formation of aberrant products.

Manipulation of the cyclization template by site-directed mutagenesis can redirect the biosynthetic trajectory of a terpenoid cyclase. This result can be achieved by modification of active site contour residues (*34*) or of residues that are more distant from the active site (*35*). With EIZS, two different strategies have been employed to manipulate the cyclization template. Mutagenesis of metal-binding residues appears to have an only modest effect on the cyclization template such that the fidelity of epi-isozizaene biosynthesis is not significantly compromised. Indeed, certain amino acid substitutions involving the Mg^{2+}-binding residues, such as D100N, N240D, S244A, and E248D, actually lead to increased proportions of epi-isozizaene and lower levels of the alternative sesquiterpene products, although with significantly decreased overall catalytic efficiency (Figure 6) (*14*). Mutagenesis of residues in closer contact with the farnesyl moiety or the derived cations (and which therefore contribute directly to the active site contour) significantly compromises the fidelity of epi-isozizaene biosynthesis (Figure 6), with the F198A substitution completely suppressing epi-isozizaene formation and redirecting the cyclization cascade toward the generation of alternative acyclic, monocyclic, and bicyclic sesquiterpenes. Thus, remolding the active site contour by mutagenesis opens up new cyclization trajectories while closing off old ones.

The appearance of low levels of new or alternative cyclization products resulting from mutagenesis of the active site contour in a terpenoid cyclase may reflect past or future evolutionary potential; i.e., catalytic promiscuity in enzyme function may provide a "toehold of evolution" (*36*). The evolution of biosynthetic diversity in this family of enzymes is achieved by simply remolding the active site contour to promote one cyclization pathway while suppressing hundreds of others, and it is notable that this is readily achieved by only a handful of amino acid substitutions. This work represents the first step in deciphering the relationship between the structure of the EIZS active site and its biosynthetic specificity as a product-like template for terpenoid cyclization reactions: the three-dimensional contour of the active site can be remolded to better fit another product and disfavor others, even to the point of excluding epi-isozizaene formation. That the biosynthetic specificity of a terpenoid cyclase is so sensitive to and so readily manipulated by minimal mutagenesis in nature or in the laboratory will likely contribute to the growing structural and stereochemical diversity of the terpenome.

ACKNOWLEDGMENT

We thank the National Synchrotron Light Source at Brookhaven National Laboratory (beamline X29A) and the Advanced Photon Source at Argonne National Laboratory (NE-CAT beamline 24-ID-C) for access to X-ray crystallographic data collection facilities. We thank Dr. Wayne Chou for providing FPP and assistance with GC−MS experiments and Cristina Virgilio for assistance with protein preparation.

REFERENCES

1. Lesburg, C. A., Caruthers, J. M., Paschall, C. M., and Christianson, D. W. (1998) Managing and manipulating carbocations in biology: Terpenoid cyclase structure and mechanism. *Curr. Opin. Struct. Biol. 8*, 695–703.
2. Christianson, D. W. (2006) Structural biology and chemistry of the terpenoid cyclases. *Chem. Rev. 106*, 3412–3442.
3. Christianson, D. W. (2008) Unearthing the roots of the terpenome. *Curr. Opin. Chem. Biol. 12*, 141–150.
4. Tholl, D. (2006) Terpene synthases and the regulation, diversity and biological roles of terpene metabolism. *Curr. Opin. Plant Biol. 9*, 297–304.
5. Austin, M. B., O'Maille, P. E., and Noel, J. P. (2008) Evolving biosynthetic tangos negotiate mechanistic landscapes. *Nat. Chem. Biol. 4*, 217–222.
6. Lesburg, C. A., Zhai, G., Cane, D. E., and Christianson, D. W. (1997) Crystal structure of pentalenene synthase: Mechanistic insights on terpenoid cyclization reactions in biology. *Science 277*, 1788–1789.
7. Starks, C. M., Back, K., Chappell, J., and Noel, J. P. (1997) Structural basis for cyclic terpene biosynthesis by tobacco 5-epi-aristolochene synthase. *Science 277*, 1815–1820.
8. Caruthers, J. M., Kang, I., Rynkiewicz, M. J., Cane, D. E., and Christianson, D. W. (2000) Crystal structure determination of aristolochene synthase from the blue cheese mold, *Penicillium roqueforti*. *J. Biol. Chem. 275*, 25533–25539.
9. Rynkiewicz, M. J., Cane, D. E., and Christianson, D. W. (2001) Structure of trichodiene synthase from *Fusarium sporotrichioides* provides mechanistic inferences on the terpene cyclization cascade. *Proc. Natl. Acad. Sci. U.S.A. 98*, 13543–13548.
10. Shishova, E. Y., Di Costanzo, L., Cane, D. E., and Christianson, D. W. (2007) X-ray crystal structure of aristolochene synthase from *Aspergillus terreus* and evolution of templates for the cyclization of farnesyl diphosphate. *Biochemistry 46*, 1941–1951.
11. Gennadios, H. A., Gonzalez, V., Di Costanzo, L., Li, A., Yu, F., Miller, D. J., Allemann, R. K., and Christianson, D. W. (2009) Crystal structure of (+)-δ-cadinene synthase from *Gossypium arboreum* and evolutionary divergence of metal binding motifs for catalysis. *Biochemistry 48*, 6175–6183.
12. Tarshis, L. C., Yan, M., Poulter, C. D., and Sacchettini, J. C. (1994) Crystal structure of recombinant farnesyl diphosphate synthase at 2.6-Å resolution. *Biochemistry 33*, 10871–10877.
13. Lin, X., Hopson, R., and Cane, D. E. (2006) Genome mining in *Streptomyces coelicolor*: Molecular cloning and characterization of a new sesquiterpene synthase. *J. Am. Chem. Soc. 128*, 6022–6023.
14. Lin, X., and Cane, D. E. (2009) Biosynthesis of the sesquiterpene antibiotic albaflavenone in *Streptomyces coelicolor*. *J. Am. Chem. Soc. 131*, 6332–6333.
15. Zhao, B., Lin, X., Lei, L., Lamb, D. C., Kelly, S. L., Waterman, M. R., and Cane, D. E. (2008) Biosynthesis of the sesquiterpene antibiotic albaflavenone in *Streptomyces coelicolor* A3(2). *J. Biol. Chem. 283*, 8183–8189.
16. Gürtler, H., Pedersen, R., Anthoni, U., Christophersen, C., Nielsen, P. H., Wellington, E. M., Pedersen, C., and Bock, K. (1994) Albaflavenone, a sesquiterpene ketone with a zizaene skeleton produced by a streptomycete with a new rope morphology. *J. Antibiot. 47*, 434–439.
17. Otwinowski, Z., and Minor, M. (1997) Processing of X-ray diffraction data collected in oscillation mode. *Methods Enzymol. 276*, 307–326.
18. Vonrhein, C., Blanc, E., Roversi, P., and Bricogne, G. (2007) Automated structure solutoin with autoSHARP. *Methods Mol. Biol. 364*, 215–230.
19. Brunger, A. T. (2007) Version 1.2 of the Crystallography and NMR system. *Nat. Protoc. 2*, 2728–2733.
20. Jones, T. A., Zou, J. Y., Cowan, S. W., and Kjeldgaaard, M. (1991) Improved methods for building protein models in electron density maps and the location of errors in these models. *Acta Crystallogr. A47*, 110–119.
21. Emsely, P., and Cowtan, K. (2004) Coot: Model-building tools for molecular graphics. *Acta Crystallogr. D60*, 2126–2132.
22. Adams, P. D., Grosse-Kunstleve, R. W., Hung, L. W., Ioerger, T. R., McCoy, A. J., Moriarty, N. W., Read, R. J., Sacchettini, J. C., Sauter, N. K., and Terwilliger, T. C. (2002) PHENIX: Building new software for automated crystallographic structure determination. *Acta Crystallogr. D58*, 1948–1954.
23. Storoni, L. C., McCoy, A. J., and Read, R. J. (2004) Likelihood-enhanced fast rotation functions. *Acta Crystallogr. D60*, 432–438.
24. Harangi, J. (2003) Retention index calculation without n-alkanes: The virtual carbon number. *J. Chromatogr., A 993*, 187–195.
25. Whittington, D. A., Wise, M. L., Urbansky, M., Coates, R. M., Croteau, R. B., and Christianson, D. W. (2002) Bornyl diphosphate synthase: Structure and strategy for carbocation manipulation by a terpenoid cyclase. *Proc. Natl. Acad. Sci. U.S.A. 99*, 15375–15380.
26. Hyatt, D. C., Youn, B., Zhao, Y., Santhamma, B., Coates, R. M., Croteau, R. B., and Kang, C. (2007) Structure of limonene synthase, a simple model for terpenoid cyclase catalysis. *Proc. Natl. Acad. Sci. U.S.A. 104*, 5360–5365.
27. Seemann, M., Zhai, G., de Kraker, J. W., Paschall, C. M., Christianson, D. W., and Cane, D. E. (2002) Pentalenene synthase. Analysis of active site residues by site-directed mutagenesis. *J. Am. Chem. Soc. 124*, 7681–7689.

28. Ma, J. C., and Dougherty, D. A. (1997) The cation-π interaction. *Chem. Rev. 97*, 1303–1324.
29. Jenson, C., and Jorgensen, W. L. (1997) Computational investigations of carbenium ion reactions relevant to sterol biosynthesis. *J. Am. Chem. Soc. 119*, 10846–10854.
30. Vedula, L. S., Zhao, Y., Coates, R. M., Koyama, T., Cane, D. E., and Christianson, D. W. (2007) Exploring biosynthetic diversity with trichodiene synthase. *Arch. Biochem. Biophys. 466*, 260–266.
31. Shishova, E. Y., Yu, F., Miller, D. J., Faraldos, J. A., Zhao, Y., Coates, R. M., Allemann, R. K., Cane, D. E., and Christianson, D. W. (2008) X-ray crystallographic studies of substrate binding to aristolochene synthase suggest a metal ion binding sequence for catalysis. *J. Biol. Chem. 283*, 15431–15439.
32. Felicetti, B., and Cane, D. E. (2004) Aristolochene synthase: Mechanistic analysis of active site residues by site-directed mutagenesis. *J. Am. Chem. Soc. 126*, 7212–7221.
33. Hong, Y. J., and Tantillo, D. J. (2009) Consequences of conformational preorganization in sesquiterpene biosynthesis: Theoretical studies on the formation of the bisabolene, curcumene, acoradiene, zizaene, cedrene, duprezianene, and sesquithuriferol sesquiterpenes. *J. Am. Chem. Soc. 131*, 7999–8015.
34. Yoshikuni, Y., Ferrin, T. E., and Keasling, J. D. (2006) Designed divergent evolution of enzyme function. *Nature 440*, 1078–1082.
35. O'Maille, P. E., Malone, A., Dellas, N., Andes Hess, B. J., Smentek, L., Sheehan, I., Greenhagen, B. T., Chappell, J., Manning, G., and Noel, J. P. (2008) Quantitative exploration of the catalytic landscape separating divergent plant sesquiterpene synthases. *Nature 4*, 617–623.
36. Petsko, G. A., Kenyon, G. L., Gerlt, J. A., Ringe, D., and Kozarich, J. W. (1993) On the origin of enzymatic species. *Trends Biochem. Sci. 18*, 372–376.